Acta Oceanol. Sin., 2022, Vol. 41, No. 7, P. 42–53
https://doi.org/10.1007/s13131-021-1971-3
http://www.aosocean.com
E-mail: ocean2@hyxb.org.cn

Submesoscale-enhanced filaments and frontogenetic mechanism within mesoscale eddies of the South China Sea

Ruixi Zheng[1, 2], Zhiyou Jing[1, 3*]

[1] State Key Laboratory of Tropical Oceanography, South China Sea Institute of Oceanology, Chinese Academy of Sciences, Guangzhou 510301, China

[2] University of Chinese Academy of Sciences, Beijing 100049, China

[3] Southern Marine Science and Engineering Guangdong Laboratory (Guangzhou), Guangzhou 511458, China

Received 12 June 2021; accepted 5 October 2021

Abstract

Submesoscale activity in the upper ocean has received intense studies through simulations and observations in the last decade, but in the eddy-active South China Sea (SCS) the fine-scale dynamical processes of submesoscale behaviors and their potential impacts have not been well understood. This study focuses on the elongated filaments of an eddy field in the northern SCS and investigates submesoscale-enhanced vertical motions and the underlying mechanism using satellite-derived observations and a high-resolution (~500 m) simulation. The satellite images show that the elongated highly productive stripes with a typical lateral scale of ~25 km and associated filaments are frequently observed at the periphery of mesoscale eddies. The diagnostic results based on the 500 m-resolution realistic simulation indicate that these submesoscale filaments are characterized by cross-filament vertical secondary circulations with an increased vertical velocity reaching O(100 m/d) due to submesoscale instabilities. The vertical advections of secondary circulations drive a restratified vertical buoyancy flux along filament zones and induce a vertical heat flux up to 110 W/m^2. This result implies a significant submesoscale-enhanced vertical exchange between the ocean surface and interior in the filaments. Frontogenesis that acts to sharpen the lateral buoyancy gradients is detected to be conducive to driving submesoscale instabilities and enhancing secondary circulations through increasing the filament baroclinicity. The further analysis indicates that the filament frontogenesis detected in this study is not only derived from mesoscale straining of the eddy, but also effectively induced by the subsequent submesoscale straining due to ageostrophic convergence. In this context, these submesoscale filaments and associated frontogenetic processes can provide a potential interpretation for the vertical nutrient supply for phytoplankton growth in the high-productive stripes within the mesoscale eddy, as well as enhanced vertical heat transport.

Key words: submesoscale process, vertical exchange, frontogenesis, South China Sea

Citation: Zheng Ruixi, Jing Zhiyou. 2022. Submesoscale-enhanced filaments and frontogenetic mechanism within mesoscale eddies of the South China Sea. Acta Oceanologica Sinica, 41(7): 42–53, doi: 10.1007/s13131-021-1971-3

1 Introduction

Mesoscale eddies with a typical horizontal scale of approximately 100 km greatly contribute to the transports of heat, mass, and biogeochemical tracers in the open ocean (Bryden and Brady, 1989; Chelton et al., 2011a; Dong et al., 2014; Zhang et al., 2014; McGillicuddy, 2016). However, the upwelling induced by mesoscale eddies may only account for 20%–30% of new production (Martin, 2003; McGillicuddy et al., 2003). Meanwhile, submesoscale-induced vertical advection is considered as an important process that fills the gap in vertical transport (Lévy et al., 2001; Omand et al., 2015; Mahadevan, 2016). Submesoscale motions characterized by O(1) Rossby and Richardson numbers can induce large vertical velocities, which can be one order of magnitude greater than that of mesoscale eddies, thereby efficiently enhancing vertical exchanges in the upper ocean (Klein and Lapeyre, 2009; Klymak et al., 2016; Su et al., 2020).

Submesoscale activities are ubiquitous in the eddy-active northern South China Sea (SCS), shown by recent simulations and observations (Dong and Zhong, 2020; Lin et al., 2020; Zheng et al., 2020). In this region, most of the eddies travel southwestward along the continental slope with a propagation speed close to that of baroclinic Rossby waves, before they die near the Xisha Islands (Wang et al., 2008; Chen et al., 2011; Nan et al., 2011). These energetic eddies provide favorable conditions for the occurrence of submesoscale behavior (Lapeyre and Klein, 2006; Dong and Zhong, 2018; Zhang et al., 2020). Submesoscale-permitting observations and simulations suggest that the vertical transport induced by submesoscale ageostrophic processes is at least one order of magnitude larger than mesoscale eddies in winter (Zhong et al., 2017). Moreover, *in-situ* microstructure observations show that the elevated turbulent dissipation rate at the eddy periphery is closely connected with the enhancement of

Foundation item: The National Natural Science Foundation of China under contract Nos 92058201, 41776040, 41830538 and 41949907; the Talents Team Project of Southern Marine Science and Engineering Guangdong Laboratory (Guangzhou) under contract No. GML2019ZD0303; the Program of Chinese Academy of Sciences under contract Nos ZDBS-LY-DQC011, ZDRW-XH-2019-2, XDA15020901 and ISEE2021PY01.

*Corresponding author, E-mail: jingzhiyou@scsio.ac.cn

submesoscale activities (Yang et al., 2017). Also, energy budget analyses indicate that the submesoscale motion may be a dominant dissipation mechanism in anticyclonic eddies (Zhang et al., 2016; Yang et al., 2019).

At the periphery of mesoscale eddies, elongated filaments and density fronts in 10 km wide are common features at the submesoscale, which can be frequently detected from satellite images (Munk et al., 2000; Klein et al., 2011; Zhang and Qiu, 2020) and *in-situ* observations (Read et al., 2007; Adams et al., 2017; Tang et al., 2021; Tarry et al., 2021). With different water properties, the Kuroshio intrusion water and local water in the northern SCS likely be advected and elongated at the eddy periphery by eddy current, providing a favorable condition to the generation of filaments. Fine-scale *in-situ* observations in the SCS show that the plankton biomass can be significantly increased in these regions (Guo et al., 2017; Li et al., 2017; Li et al., 2021). The submesoscale processes at filaments are considered to substantially contribute the vertical transport within the northern SCS eddies (Zhong et al., 2017). However, the dynamical processes of these submesoscale activities and their potential mechanisms driving enahnced vertical transport have not been well understood in the SCS.

In this study, we focus on elongated filaments in the mesoscale eddy and examine submesoscale-enhanced vertical motions and underlying mechanism, using high-resolution (~1 km) satellite observations and a 500 m-resolution numerical simulation. Section 2 describes the satellite data, model setup, and diagnostic methods. The submesoscale features within the eddy field is detailed in Section 3. Section 4 examines the enhanced vertical secondary circulation associated with frontal submesoscale instabilities. As an important mechanism for the filament (Lapeyre and Klein, 2006; Gula et al., 2014), the potential frontogenetic mechanism is further analyzed in Section 5. Finally, Section 6 is the summary.

2 Data and methods

2.1 *Satellite data*

Daily sea level anomaly (SLA) and geostrophic velocity anomaly data are used in this study, which are obtained from the Delayed-Time Reference Series product provided by Archiving, Validation, and Interpretation of Satellite Oceanographic data (AVISO). Spatial band-pass filtering with a cutoff period of 30–120 d is utilized to minimize the noise of mesoscale eddies (Chelton et al., 2011b; Qiu and Chen, 2010). The climatological winter eddy kinetic energy (EKE $= u_{ga}^2 + v_{ga}^2$ with the geostrophic velocity anomaly (u_{ga}, v_{ga})) is obtained from 1993 to 2020 to evaluate the mesoscale variability in the northern SCS (Fig. 1a).

The trajectories of mesoscale eddies migrating from the west of the Luzon Strait to the eastern Hainan Island in the winters from 1993 to 2020 are obtained from the Mesoscale Eddy Trajectories Atlas product (META3.1exp Delayed-Time allsat version). This multi-mission altimetry-derived eddy trajectory dataset is produced by the Ssalto/Duacs and distributed by AVISO+ with support from the Centre National d'Etudes Spatiales, in collaboration with the Mediterranean Institute for Advanced Studies (https://doi.org/10.24400/527896/a01-2021.001). The anticyclonic and cyclonic eddies in this dataset are detected by searching

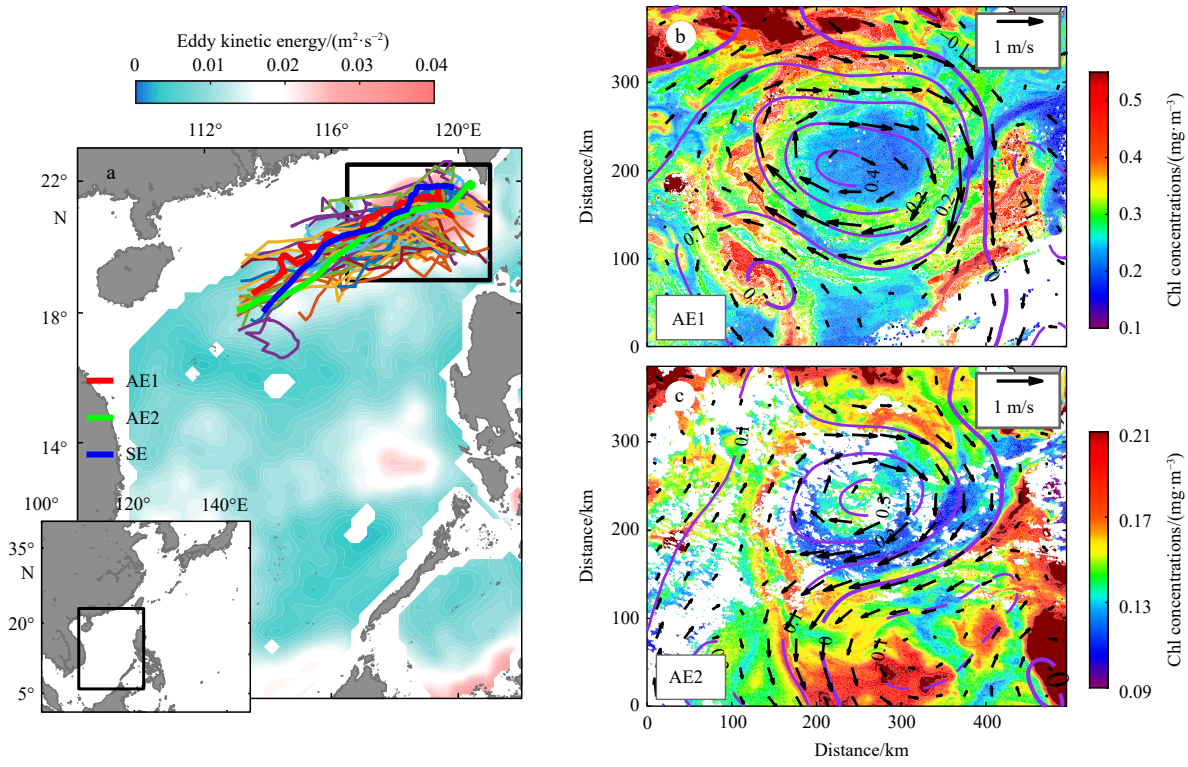

Fig. 1. Climatological map of eddy kinetic energy (shading) and the trajectory of mesoscale eddies (color lines) in winter (December, January, February) from 1993 to 2020 in the South China Sea (a); satellite-observed chlorophyll (Chl) concentrations for the AE1 on December 4, 2013 (b) and the AE2 on November 8, 2015 (c). The data in the shelf (<500 m) have been removed. The red, green, and blue bold lines in a show the eddy case trajectory of AE1, AE2 and simulated eddy SE, respectively. Purple contours denote the sea level anomaly and vectors show the geostrophic velocity anomaly. AE1, AE2: anticyclonic eddies.

closed contours in agreement with the defined criteria around each local maximum and minimum of SLA field (Mason et al., 2014). The trajectories and characteristics (e.g., amplitudes, radii, and speeds) of eddies are further estimated after performing the eddy detection on several consecutive days.

Fine-resolution satellite images of the chlorophyll (Chl) concentration and sea surface temperature are derived from Suomi-NPP Visible Infrared Imaging Radiometer Suite and Terra/Aqua Moderate Resolution Imaging Spectroradiometer sensors. With a spatial resolution of approximately 1 km, the ungridded Level-2 product provided by the NASA Goddard Space Flight Center is used in this study. However, the quality of the satellite images for filaments is always poor because of the corruption of large cloud coverage in the northern SCS. Thus, we synthesize satellite images over 1 d using the inverse distance-weighted method to maximize the available coverage. Consequently, several submesoscale filaments are observed within the two anticyclonic eddies (Figs 1b, c).

2.2 *High-resolution simulation*

The model used in this study is the Regional Oceanic Modeling System (ROMS), which has been widely used in oceanic studies (Shchepetkin and McWilliams, 2005). To examine the submesoscale features at the periphery of eddies, a nesting approach is adopted with successive horizontal grid nesting refinements from a parent grid with a resolution of Δx≈7.5 km (ROMS0) to refined child grids with resolutions of Δx≈1.5 km (ROMS1) and Δx≈500 m (ROMS2). The nesting approach is an online, one-way nesting from coarser to finer models, without feedback from the child solution to the parent model (Penven et al., 2006). The bottom topographies for both parent and child domains are constructed from the General Bathymetric Chart of the Oceans dataset, which is comprised of a 30 arc-sec (~1 km) gridded global relief data produced by the British Oceanographic Data Center (BODC). Utilizing terrain-following S-coordinates, the same vertical grids for all simulations are 60 σ-levels, which are concentrated near the surface and bottom with parameters $\theta_s = 7$ and $\theta_b = 2$, respectively. The vertical subgrid boundary-layer mixing is parameterized using a K-profile parameterization (KPP), which is widely used in ocean models (Large et al., 1994). The boundary and initial information for the parent domain are derived from the monthly climatology of the Simple Ocean Data Assimilation reanalysis dataset (Carton and Giese, 2008), which is distributed by the Asia-Pacific Data-Research Center (APDRC). The parent and child simulations are forced by the climatological surface atmospheric forcing, including wind stress, heat and freshwater fluxes, and lateral oceanic forcing. The daily climatological wind field is derived by averaging daily surface wind of the Quick Scatterometer dataset from September 1999 to October 2009 (Risien and Chelton, 2008), which has a spatial resolution of 0.25°×0.25°. The heat and freshwater atmospheric forcing data are provided by the monthly climatology of the International Comprehensive Ocean-Atmosphere Data Set at a coarse resolution of 1°×1° (da Silva et al., 1994; Woodruff et al., 2011), as distributed by the APDRC. More details regarding the model setup can be found in the model description by Jing et al. (2021).

The parent model ROMS0 covering the Northwest Pacific (not shown) is spun up for a 20-year period, and then run for an additional two years with a daily output. The ROMS1 model encompassing the SCS region (2°–25°N, 102°–127°E) and the ROMS2 model covering the northern SCS (15°–24°N, 109°–121°E) are successively nested with boundary conditions interpolated from the ROMS0 in the last two years, as shown in Fig. 2. The modeling results (e.g., regional circulation, thermohaline structure, mixed layer depth (MLD), and energy level of mesoscale eddies) have been validated against satellite measurements, reanalysis datasets, and available historical *in-situ* observations in the SCS (Jing et al., 2021). Comparisons between multiple platforms show that the simulations are sufficiently accurate to characterize the climatological conditions of the SCS upper ocean. The results of the ROMS1 and ROMS2 models have some difference from the observations because of the climatological forcing and one-way nesting. The ROMS2 model exhibits active submesoscale vorticity filaments on a lateral scale of approximately 25 km at the surface.

2.3 *Dynamical diagnostics for submesoscale filament*

Frontal sharpness is a quantitative indicator of a filament with a much stronger lateral buoyancy gradient than the ambient region, and is represented by $M^4 = |\nabla_h b|^2$ (Gula et al., 2014), where $\nabla_h = \left(\frac{\partial}{\partial x}, \frac{\partial}{\partial y}\right)$ is the lateral gradient and $b = -g\rho/\rho_0$ is the buoyancy, in which g is the gravity, ρ is the density, and ρ_0 is the reference density. The vertical stretching and horizontal convergence in the filaments are shown by the vertical relative vorticity $\zeta = v_x - u_y$ and divergence $\delta = u_x + v_y$ respectively, where u and v are the zonal and meridional velocities. The total flow $\boldsymbol{u}_3 = (u, v, w)$ and buoyancy b are decomposed into the background and submesoscale component by a spatial average as $\boldsymbol{u}_3 = \bar{\boldsymbol{u}}_3 + \boldsymbol{u}'_3$ and $b = \bar{b} + b'$. The average scale is estimated by the wavelength corresponding to the fastest-growing mode of the mixed layer instability $L = 2\pi NH\sqrt{1 + Ri^{-1}}/f \approx 25$ km (Stone, 1966; Boccaletti et al., 2007), where the region-averaged buoyancy frequency $N = \sqrt{\bar{b}_z} = \sqrt{-(g/\rho_0)\,\partial\rho/\partial z} \approx 2 \times 10^{-3}$ s^{-1}, the MLD is $H \approx 65$ m, balanced Richardson number $Ri = 1$, and the Coriolis frequency is $f = 4.7 \times 10^{-5}$ s^{-1} in the study region, which correspond to the lateral scale of filaments. The vertical heat flux induced by submesoscale processes is estimated using $Q_t = \rho_0 c_p \langle w'T' \rangle$, where the sea water specific heat capacity c_p is a constant (3 850 J/(kg·°C)) and $\langle\,\rangle$ denotes a regional average. The vertical buoyancy flux VBF $= \langle w'b' \rangle$ is estimated to show the tendency of restratification in the filament.

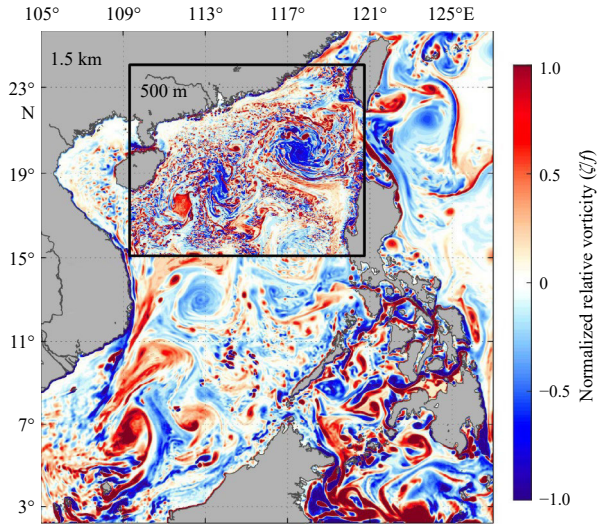

Fig. 2. Snapshot of surface Rossby number ($Ro = \zeta/f$) in the nested South China Sea winter simulations. The resolution of ROMS1 is 1.5 km. The boundary of the second nested domain with Δx=500 m is delineated by a black box.

Elongated buoyancy filaments can be super-exponentially sharpened by strain-induced frontogenesis (McWilliams et al., 2009a). The horizontal strain rate is defined as follows:

$$St = \sqrt{St_n^2 + St_s^2} = \sqrt{(u_x - v_y)^2 + (u_y + v_x)^2}, \quad (1)$$

where the normal strain St_n and shear strain St_s denote the horizontal expansion and shear rate, respectively. The maximum stretching direction of the deformed flow is denoted by the direction of the principal strain axis: $\theta_p = \arctan(St_s/St_n)/2$ (Gula et al., 2014). The angle between the principal axis of strong strain and the filamentary axis is smaller than $\pi/4$ during the strain-induced frontogenesis.

Frontogenesis can be driven by large- and mesoscale strain (Spall, 1995; McWilliams et al., 2009b) and boundary-layer turbulence (Gula et al., 2014; McWilliams et al., 2015). The horizontal advection of mesoscale and large-scale flows is expected to initiate the frontogenesis process (Capet et al., 2008; Shakespeare and Taylor, 2013). This effect can be diagnosed by advective frontogenetic tendency F_{adv} (Hoskins, 1982):

$$\frac{D}{Dt}|\nabla_h b|^2 \approx F_{adv} = (-b_x \nabla_h u - b_y \nabla_h v) \cdot \nabla_h b. \quad (2)$$

Considering the vertical mixing in the mixed layer (ML), the filament frontogenesis at a later stage can be induced by turbulent vertical momentum mixing through cross-filament secondary circulations, referred to the turbulence thermal wind balance (Gula et al., 2014; Sullivan and McWilliams, 2018). According to the ageostrophic secondary circulation and frontogenetic tendency (SCFT) theoretical framework (McWilliams, 2017), the terms contributing to the frontogenesis associated with the local buoyancy anomaly b' can be evaluated as

$$F = \frac{1}{2}\frac{D(\nabla b')^2}{Dt} = F_g + F_a + F_\alpha + F_{\kappa_v}, \quad (3)$$

where

$$F_g = \nabla_h b' \cdot J[\nabla_h \psi_g, b'] \quad (4)$$

is the geostrophic self-straining tendency term with the geostrophic stream function ψ_g ($u_g = -\partial_y \psi_g$, $v_g = \partial_x \psi_g$, $b' = f\partial_z \psi_g$) and the horizontal Jacobian operator $J[p,q] = \partial_x p \partial_y q - \partial_y p \partial_x q$. The frontogenetic rate related to ageostrophic buoyancy advection of secondary circulations is

$$F_a = F_u + F_w = -[\nabla_h b' \cdot \nabla_h]\boldsymbol{u}_{a3} \cdot \nabla b' - \bar{N}^2 \nabla_h w' \cdot \nabla_h b', \quad (5)$$

where F_u and F_w are the two ageostrophic horizontal strain terms associated with horizontal and vertical advection, respectively. The mean stratification frequency is defined as $\bar{N}^2 = \partial_z \bar{b}$, and $\boldsymbol{u}_{a3} = (\boldsymbol{u}_a, w')$ refers to the submesoscale ageostrophic velocity. The local ageostrophic horizontal velocity $\boldsymbol{u}_a$ can be derived from the submesoscale horizontal velocity by subtracting the local geostrophic velocity $\boldsymbol{u}_g$. The term implicating the frontogenetic effect of external deformation can be expressed as

$$F_\alpha = \alpha\left[(\partial_x b')^2 - (\partial_y b')^2\right]. \quad (6)$$

The external strain α is the mesoscale horizontal strain rate, which has a typical magnitude of 10^{-5} s^{-1} in mesoscale eddies (McWilliams, 2017). The effect of the boundary-layer vertical buoyancy mixing is as follows:

$$F_{\kappa_v} = [\nabla_h b' \cdot \nabla_h]\,\partial_z(\kappa_v \partial_z b'), \quad (7)$$

where κ_v is the turbulent vertical mixing coefficient from the KPP scheme (Large et al., 1994).

Ertel potential vorticity (PV) denoting flow stability is another widely discussed feature for a front or filament. Under the surface forcing and vertical momentum mixing, PV is prone to reach negative ($qf < 0$) at the surface. When this occurs, the ocean can become susceptible to several submesoscale instabilities and enhanced turbulence (Boccaletti et al., 2007; Taylor and Ferrari, 2009; Thomas et al., 2013). For filaments, the PV is defined by the Ertel PV (Hoskins, 1974),

$$q = \omega \cdot \nabla b = (f\hat{k} + \nabla \times \boldsymbol{u}) \cdot \nabla b = q_v + q_h \approx (f+\zeta)N^2 + \omega_h \cdot \nabla_h b, \quad (8)$$

where the absolute vorticity ω is composed of the vertical $(f+\zeta)$ and horizontal components $\omega_h = (v_z - w_y, w_x - u_z)$ and $\hat{k}$ is the vertical unit vector. The Ertel PV can be decomposed into vertical q_v and horizontal components q_h. q_v is associated with the vertical component of the absolute vorticity and the stratification. And q_h is attributable to the lateral buoyancy gradients and vertical shear, that is, the horizontal baroclinicity. In the northern hemisphere, q_h is always negative to compensate q_v. The baroclinic component may be non-negligible and cause a negative PV at filaments where baroclinicity is enhanced.

3 Submesoscale filaments at the eddy periphery

3.1 *Satellite-observed filaments*

Using high-resolution ocean color maps, narrow stripes with a width of ~25 km have been observed within two anticyclonic eddies AE1 (December 4, 2013) and AE2 (November 8, 2015), providing observation evidence for active submesoscale behaviors within the eddy field (Figs 1b, c). The stripes are highly productive in the oligotrophic SCS, having a much higher Chl concentration (approximately 0.1 mg/m^3) than surrounding areas. Meanwhile, the cold and warm waters outside the eddy are likely to be stirred and elongated horizontally by the eddy advection, and form filaments and fronts at the eddy periphery (Fig. 3 and vectors in Fig. 1b). The filaments and fronts are roughly aligned with these highly productive stripes. This spatial consistency suggests that the increased surface Chl concentration is dynamically associated with frontal processes.

The lateral length scale of the filament that is much smaller than the first baroclinic Rossby radius of deformation describing the horizontal scales of geostrophic processes ($R_d \approx 60$ km; Chelton et al., 1998) indicates that the filaments favor to departing from the geostrophic balance and inducing ageostrophic motions. The increased horizontal temperature gradient with a surface temperature difference of 0.1–0.5°C at the edges of filaments suggests that the filaments are conducive to frontal instabilities. Because the satellite images show only surface signals, a typical anticyclonic eddy SE similar to the observed eddies is selected to further investigate the submesoscale motions and potential dynamical mechanism in these filaments.

3.2 *Submesoscale filaments in the simulations*

The observed eddy and associated filaments are roughly re-

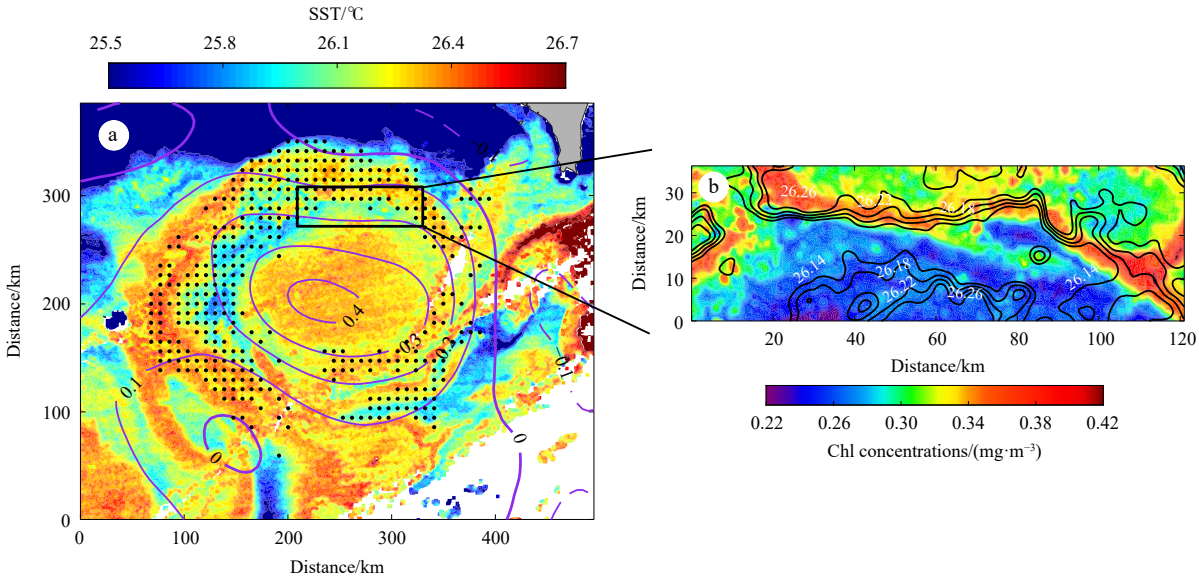

Fig. 3. Observed sea surface temperature (SST) field at the time of Fig. 1b (a); snapshot of chlorophyll (Chl) (shading) and SST (contours at an interval of 0.04°C) for the submesoscale filaments (b). Purple contours denote the sea level anomaly. Black spots show the distribution of high-productive filaments (>0.3 mg/m^3).

produced by the simulation, as shown in Fig. 4. Thermal filaments around the eddy have a similar temperature difference between the filament and ambient regions (~0.5°C), and a similar lateral scale of 10–30 km (Fig. 4a). These filaments have a mean lateral temperature gradient of approximately 0.03°C/km at the surface, and can affect through the ML (Fig. 4b). The ML-averaged frontal sharpness is increased to 1×10^{-13} s^{-4} in these regions, showing a large lateral buoyancy gradient in the filament zones (Fig. 4c). The increased relative vorticity normalized by f (i.e., Ro) indicates a departure from balanced geostrophic dynamics.

The surface snapshots of dynamic parameters show that elongated filaments with large lateral buoyancy gradients are active at the eddy periphery (Fig. 5). The lateral stretch and shear of the flows increase the horizontal straining St to $>1\times10^{-4}$ s^{-1} in the vicinity of the filaments, tending to induce frontogenesis processes. Additionally, the negative normalized divergence δ/f shows a surface convergence along the filaments zone and a peak downwelling flow beneath it. Increased by the vortex stretching, positive Ro with a maximum exceeding 5 indicates that ageostrophic motions associated with submesoscale behaviors are active in the filaments.

4 Vertical exchanges associated with secondary circulations

The stability of filamentary flows is showed by the Ertel PV q at a magnified segment of the strongest filament (Fig. 6). The Ertel PV is reduced to negative along the filament under the effect of surface cooling and strong northeast wind. The enhanced lat-

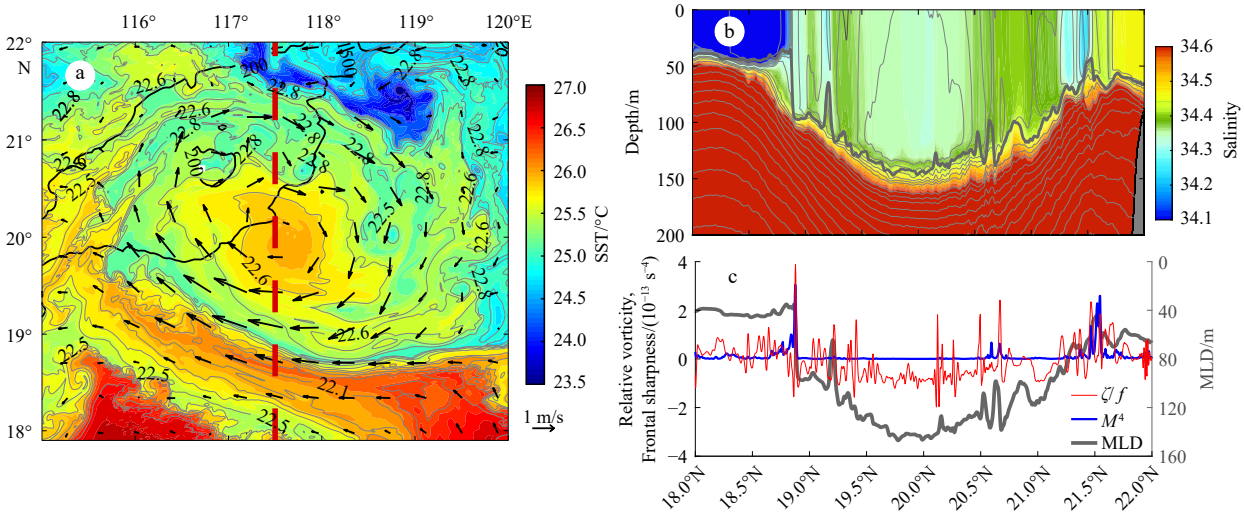

Fig. 4. Simulated sea surface temperature (SST) with horizontal velocity (vectors) (a) and a cross-eddy slice of salinity along the 117.5°E section (red dashed lines) (b) on December 18; cross-eddy profiles of normalized relative vorticity (ζ/f) and frontal sharpness (M^4) averaged over the mixed layer depth (MLD) (c). The isobaths at 200 m and 1 500 m are shown by black contours. Gray contours denote the potential density at an interval of 0.1 kg/m^3. The thick gray line denotes the MLD.

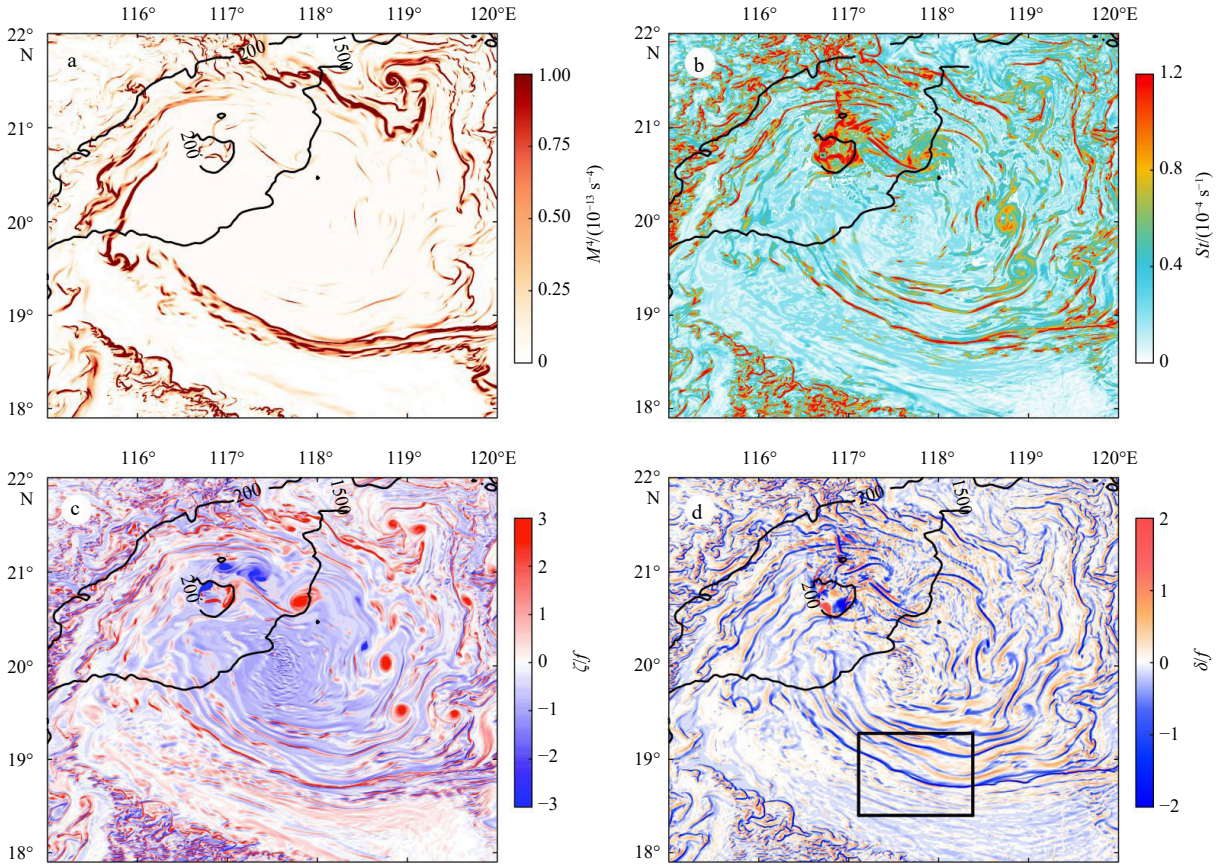

Fig. 5. Frontal sharpness M^4 (a), strain rate St (b), relative vorticity ζ normalized by f (c), and normalized divergence δ/f (d) at the surface for the mesoscale eddy shown in Fig. 4. Black contours denote the isobaths at 200 m and 1 500 m. A segment of the strongest filament is outlined by the black box.

eral buoyancy gradients are favorable to reduce the Ertel PV in the filamentary zones by increasing the absolute value of horizontal component q_h which is negative definite in the northern hemisphere. It indicates that the increased baroclinicity of filamentary flows always reduces the Ertel PV under the assumptions of geostrophic and hydrostatic balance and is conducive to frontal instability such as symmetric instability. As shown in Fig. 6d, the symmetric instability with a length scale of 0.1–2.1 km (Bachman et al., 2017, Eq. (1)) is prone to occur in the filament, indicated by negative PV and Ri from 0.25 to 0.95. Meanwhile, the mixed layer instability ranging from 2.4 km to 5.5 km (Fox-Kemper et al., 2008, Eq. (2)) may also be present in the vicinity of the filament with $Ri>1$. The active submesoscale instabilities would enhance the submesoscale flows and elevate local mixing in the filaments with a release of the geostrophic energy (Taylor and Ferrari, 2009; D'Asaro et al., 2011; Thomas et al., 2013).

To distinguish the submesoscale flow from the geostrophic flow, the flow is decomposed into a mesoscale component and a submesoscale perturbation component (Fig. 7). The submesoscale along-filament flows u_c' and cross-filament flows v_c' are about 0.1 m/s around the filament in the upper 40 m, which is one order of magnitude weaker than the velocity of quasi-geostrophic mesoscale flow (~1 m/s). However, submesoscale cross-filament flows v_c' induce a surface convergence at the axis of the filament and form two vertical secondary circulations with large submesoscale vertical flows w', shown by the vectors in Fig. 7c. The lateral lengths of secondary circulations are approximately 5 km and 10 km, respectively. The vertical pattern of this submesoscale flow field averaged along the filament is similar to the theoretical patterns of typical cold filaments given by McWilliams (2017). The weaker lateral buoyancy gradient and vortex stretching associated with deepened MLD induce an asymmetry of secondary circulations with the wider upwelling regions on the side near the eddy center.

The vertical flows are significantly energized in the filament by the submesoscale processes, shown by the submesoscale vertical velocity w' at the depth of 40 m (Fig. 7a). The submesoscale vertical flows are roughly confined in the ML and peaks at a depth of ~40 m. A strong submesoscale downwelling is induced at the axis of the filament with wider upwellings on its light sides. The instantaneous values of the downward and upward vertical velocities reach 160 m/d and 70 m/d, respectively. In contrast, the mesoscale vertical velocity $\overline{w}$ only reaches ~20 m/d and is one order of magnitude smaller than the submesoscale vertical velocity (Fig. 7b).

In response to these enhanced vertical advections of secondary circulations, a positive VBF is induced in the filament (Fig. 8b). Positive VBF peaking in the ML indicates that the secondary circulations tend to redistribute the ML buoyancy budget and restratify the ML (Fig. 8d), corresponding to the injection of surface low PV water in Fig. 6c. Meanwhile, a vertical heat flux Q_t is significantly enhanced in the filament. The filament-averaged Q_t reaches as high as 110 W/m² in the ML (Figs 8a, c), which is similar to the global estimation by Su et al. (2018). The enhanced Q_t acting to reduce the surface cooling is comparable with the sur-

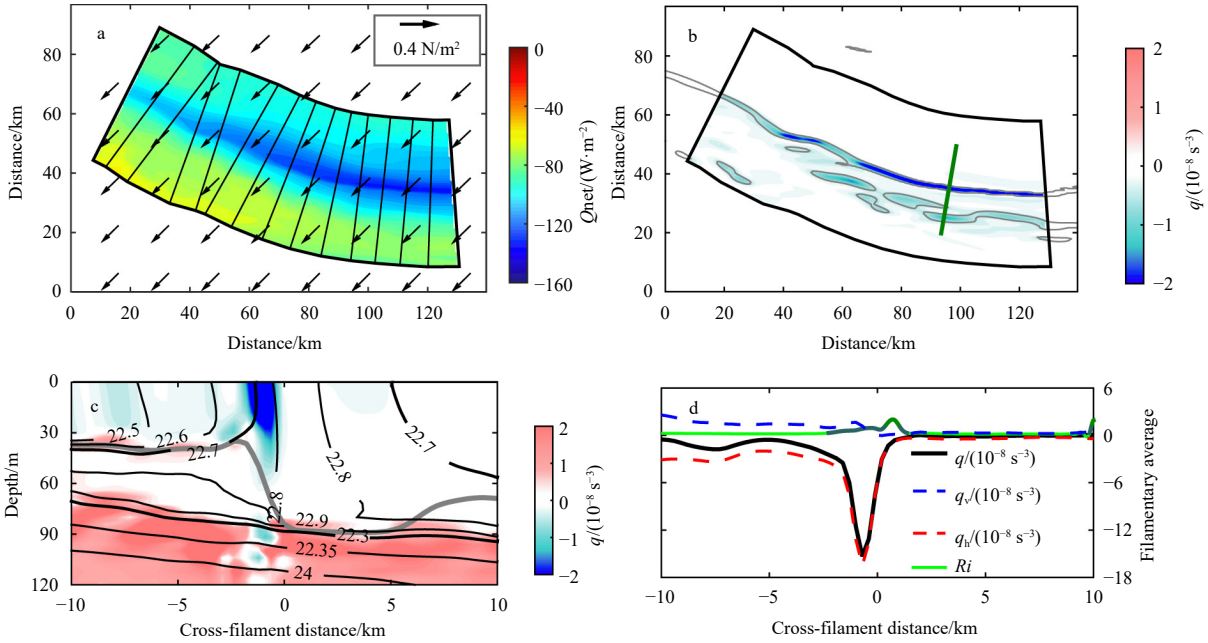

Fig. 6. Surface heat flux Q_{net} (shading) with surface wind stress (vectors) (a); snapshot (b) and vertical section (c) of Ertel potential vorticity (PV) q; filament-averaged profiles of the Ertel PV terms and Richardson number Ri (d). The cross-filament transects (shown at an interval of 30 transects) is represented by cross-filament lines in a. The filament axis is defined by the strongest frontal sharpness. Thin gray contours show the fields of frontal sharpness >1×10^{-13} s^{-4}. The isopycnal surfaces are shown by black contours (kg/m^3) and the mixed layer depth is denoted by the gray line in c. The segments of $0.25 < Ri < 0.95$ and $Ri > 1$ are shown in dark green and green, respectively.

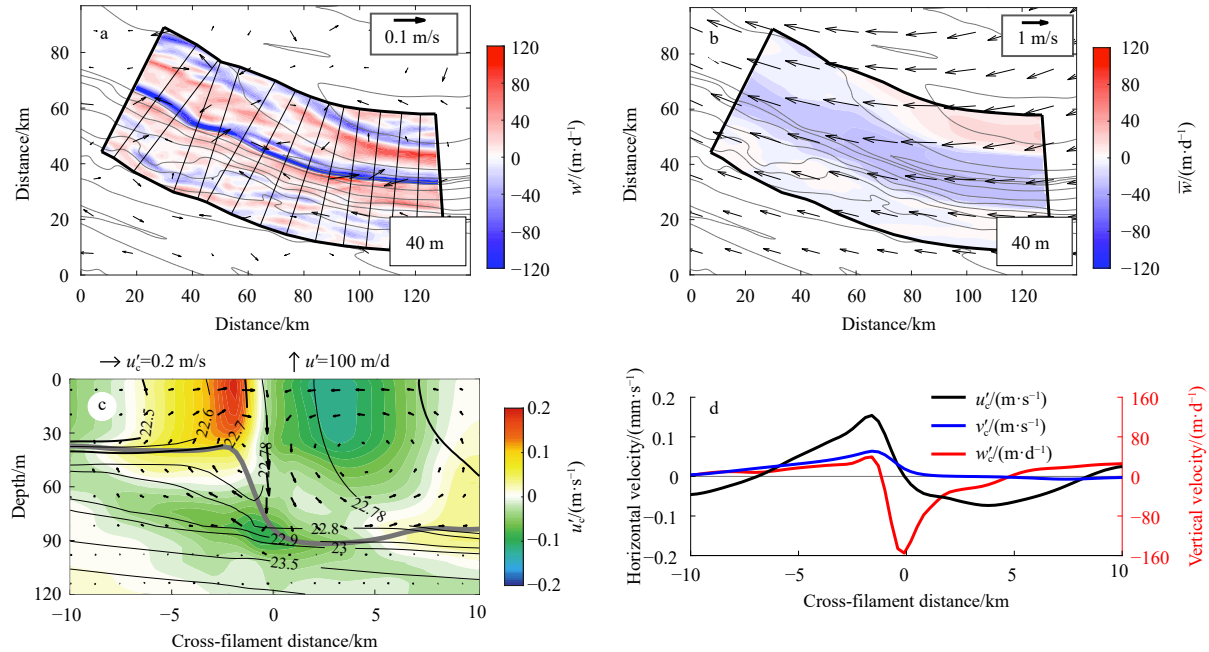

Fig. 7. Submesoscale vertical velocity w' (a) and mesoscale vertical velocity $\overline{w}$ (b) at a depth of 40 m; vertical section of submesoscale along-filament velocity u'_c averaged along the filament (c); submesoscale velocity profiles averaged over the mixed layer depth (MLD) in the filamentary region (d). Vectors in a and b denote the surface submesoscale and mesoscale flow, respectively. Gray contours show the potential density at an interval of 0.1 kg/m^3. Black contours show the isopycnal surfaces and the gray line denotes the MLD. Vectors at the section show the cross-filament v'_c and vertical velocities w' at submesoscale.

face heat flux Q_{net} which is approximately –100 W/m^2. It suggests that even the weak filament in this case can induce a large vertical heat transport by the secondary circulations, at least instantaneously.

5 Frontogenetic intensification in the filament

The along-filament principal strain axis and the surface convergence suggest that the filament is stretched along the frontal direction and compressed in the perpendicular direction (Fig. 9).

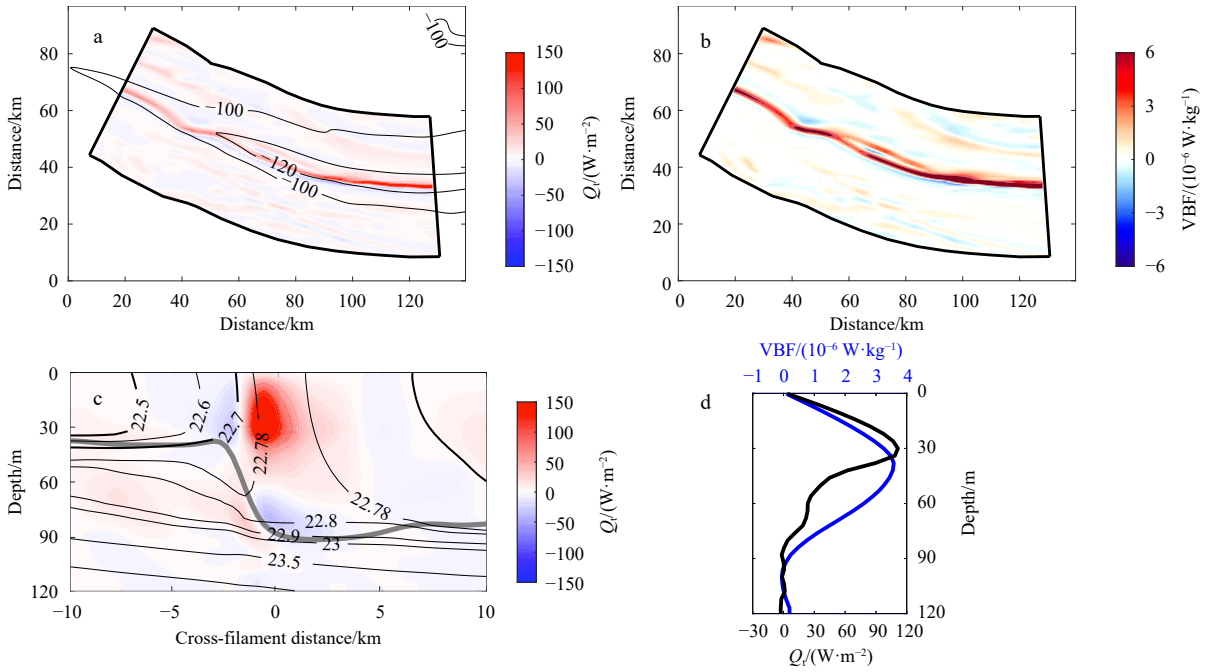

Fig. 8. Vertical heat flux Q_t (a) and vertical buoyancy flux (VBF) (b) averaged over the mixed layer; vertical section of Q_t (shading), potential density (black contours; kg/m^3) and the mixed layer depth (gray line) averaged along the filament (c); vertical profiles of Q_t and VBF averaged horizontally in the filamentary region (d). Contours in a denote the surface heat loss Q_{net}.

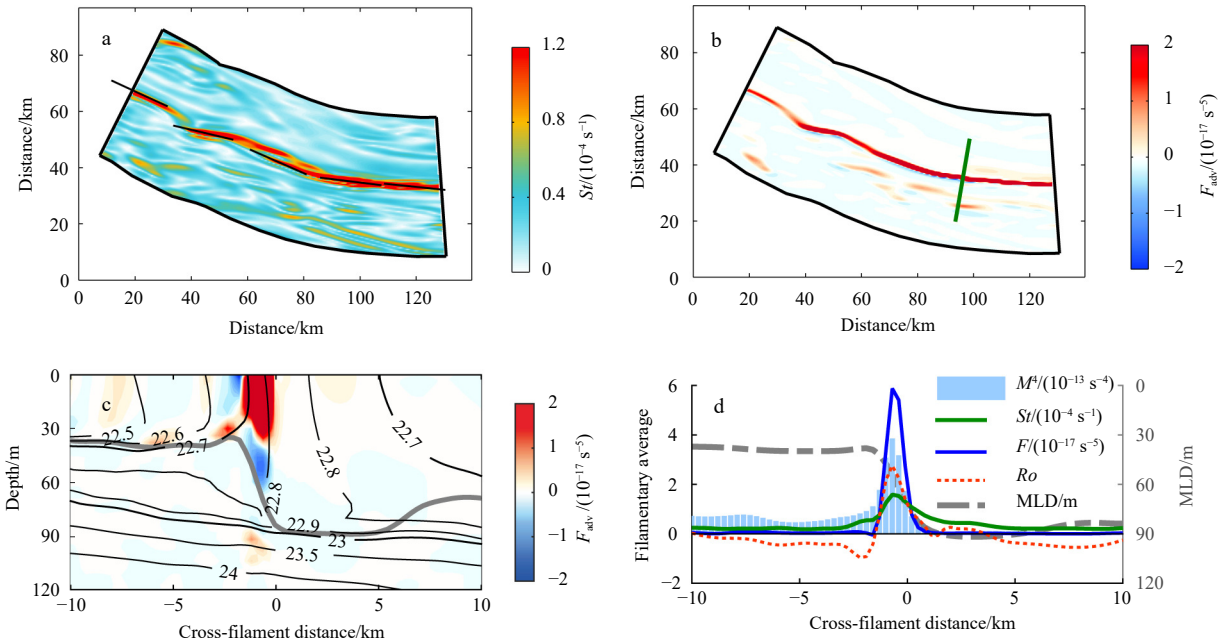

Fig. 9. Horizontal strain rate St (a) and frontogenetic tendency F_{adv} (b) at the surface; vertical distribution of frontogenetic tendency (shading) and potential density (black contours; kg/m^3) along a cross-filament section (the green line in b) (c); instantaneous filament-averaged profiles for the parameters (d). Black lines in a show the direction of the principal strain axis θ_p. The gray line denotes the mixed layer depth (MLD).

The strong strain rate and frontal sharpness indicate that strain-induced frontogenesis is responsible for the sharpened filament. Positive frontogenetic tendency F_{adv} indicates that the filament tends to be sharpened by the frontogenesis through the increasing of lateral buoyancy gradient and baroclinicity. With the PV destruction induced by the increased filamentary baroclinicity (Fig. 6), the filament stability is effectively broken down by frontogenesis in conjunction with atmospheric forcing, providing favorable conditions for the enhancement of submesoscale instabilities and secondary circulations.

As shown in Fig. 9c, the pattern of F_{adv} with the convergence-induced pattern of filaments described in Gula et al. (2014) suggests that the cross-filament convergence may play an important role in the filamentary intensification, although the signal on the

right side is weak because of weak surface straining and lateral gradients. The straining fields induced by the submesoscale flows St_s and mesoscale flows St_m are shown in Fig. 10. The shear and stretch of the westward quasi-geostrophic flows are weak in the vicinity of the filament, shown by a small strain rate St_m. In contrast, the strain rate St_s induced by the weak submesoscale flows is significantly enhanced to 1.5×10^{-4} s^{-1} and is one order of magnitude larger than the St_m. The dominant St_s indicates that the contribution of submesoscale flows may be non-negligible for the frontogenesis in this case.

According to the SCFT theoretical framework, the contributions of different frontogenetic processes for the filament frontogenesis are shown in Fig. 11. The deformation of the ageostrophic horizontal flow associated with the secondary circulations induces a strongly positive frontogenetic tendency F_u (~5×10^{-17} s^{-5}) in the filament, contributing approximately 60% of the positive total frontogenetic tendency F in this case. This positive tendency is partly balanced by the negative term F_w induced by the vertical advection. The enhanced vertical advection tends to weaken the lateral buoyancy gradients, agreeing with the tend-

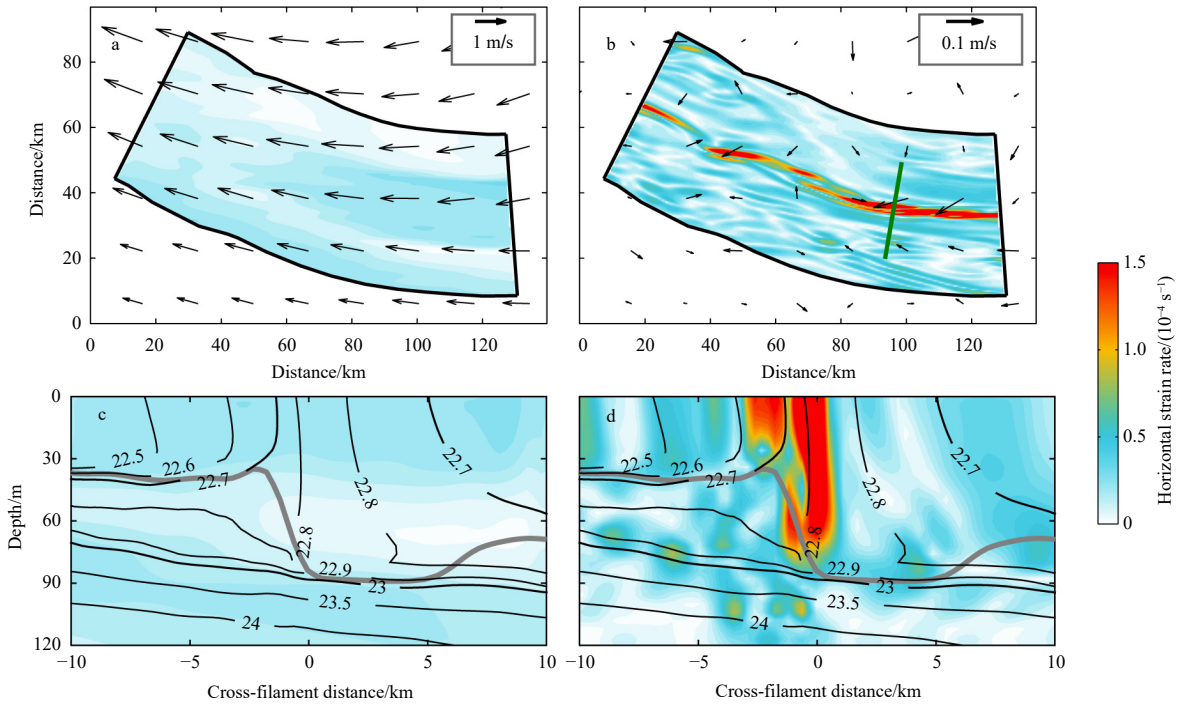

Fig. 10. Surface horizontal strain rate associated with mesoscale flows St_m (a) and submesoscale flows St_s (b); cross-filament slices of the St_m (c) and St_s (d). The horizontal mesoscale flows and submesoscale perturbations are shown by vectors. Black contours denote the isopycnal surfaces (kg/m^3). The mixed layer depth is denoted by the thick gray line.

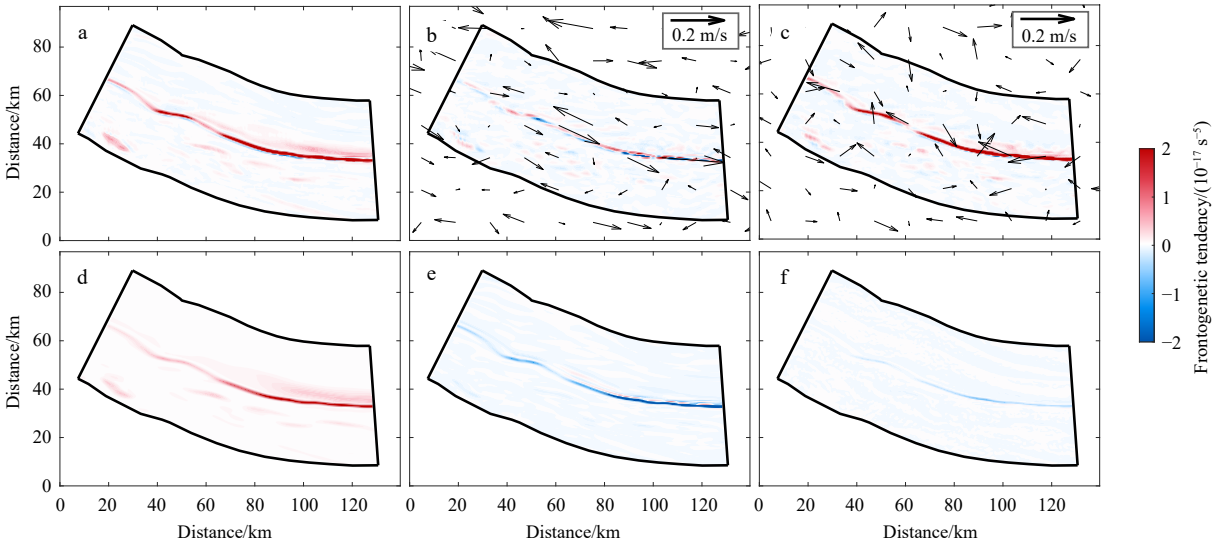

Fig. 11. Mixed layer-averaged total frontogenetic tendency F (a) and its terms caused by geostrophic self-straining F_g (b), ageostrophic horizontal advection F_u (c), external straining deformation F_α (d), ageostrophic vertical advection F_w (e), and vertical mixing F_{κ_v} (f). Vectors in b and c show the submesoscale geostrophic and ageostrophic flows, respectively.

ency of ML restratification. However, the total effect of these two terms, that is, F_a is larger than the terms related to other processes. The effect of ageostrophic secondary circulations acts as a primary influence on the buoyancy-gradient frontogenetic tendency in this study. Meanwhile, the external deformation term F_α associated with mesoscale flows has an overall positive contribution in the filament, but is one times smaller than the F_a in the present case. It indicates that the frontogenesis induced by mesoscale flows is still effective in sharpening submesoscale buoyancy gradients. The terms of geostrophic self-straining F_g and vertical mixing F_{κ_v} have relatively small contributions to the total frontogenetic tendency in this case.

6 Summary

Using high-resolution satellite observations and numerical simulations, this study focuses on the elongated filaments at the periphery of mesoscale eddy and examines the enhanced vertical motions associated with submesoscale instabilities and their underlying frontogenesis mechanism. Both the observations and high-resolution simulations indicate that the elongated stripes within the range of ~25 km are common features within SCS eddies. Narrow filaments and fronts are induced with large lateral buoyancy gradient at the edge of stripes. The flows at most of submesoscale filaments have a departure from the geostrophic balance.

Strain-induced frontogenesis is detected to rapidly enhance the lateral buoyancy gradient of the filament and reduce the PV in conjunction with atmospheric forcing, setting the precondition for submesoscale instabilities (Fig. 12). The further diagnostic results indicate that the straining associated with submesoscale flows has a comparable contribution to the growth of the filamentary baroclinicity than the mesoscale straining. Based on the SCFT theoretical framework, the contribution of each term for the total frontogenetic tendency is analyzed. The results indicate that the straining of secondary circulations is the largest contributor to the frontogenesis in this case. The straining of ageostrophic horizontal advection primarily induces the frontogenesis by the surface convergence associated with secondary circulations, while the ageostrophic vertical advection tends to arrest the frontogenesis with a restratification. Meanwhile, the external straining term associated with mesoscale flows is still effective in sharpening submesoscale buoyancy gradients but has a much weaker contribution than the secondary circulation in this study. Following the frontogenesis driven by both the lateral strain of eddy flows and boundary-layer turbulence, the filaments will become more prone to ageostrophic dynamics and thus include more rapidly growing frontal instabilities that can enhance vertical exchanges (McWilliams, 2017; Sullivan and McWilliams, 2018).

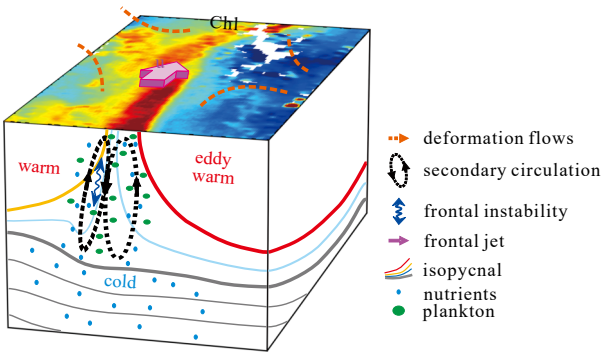

Fig. 12. Schematic diagram of the phytoplankton stripe associated with the cold filament. Shading shows the observed chlorophyll (Chl) concentration at the periphery of AE1.

The vertical secondary circulations generated by mesoscale straining are found to be enhanced by the frontogenesis and associated submesoscale instabilities along the filament zone with $O(1)$ Rossby number and increased vertical velocity of up to 100 m/d. The results show that the vertical heat transport is increased to 110 W/m^2 in the filament. The positive vertical buoyancy flux in the ML indicates a tendency of the ML restratification induced by the secondary circulations. Enhanced vertical heat and buoyancy transports imply that the vertical exchange of tracers is efficiently enhanced by the secondary circulations within the eddy field. Meanwhile, submesoscale upwellings (~ 70 m/d) favors to drawn eutrophic water from the thermocline to the surface in days which is of the same order of magnitude as the growth and uptake rates of phytoplankton (Mahadevan, 2016). Therefore, this frontogenetic mechanism and submesoscale-enhanced vertical velocities can provide a possible dynamical explanation for the observed high Chl concentrations around the filament within eddies of the SCS. With a filament strength as large as the previous observations (Hosegood et al., 2013; Thompson et al., 2016) and stimulations (Brannigan et al., 2015; Dauhajre et al., 2017) in zones without strong large-scale currents, this mechanism of filament frontogenesis may can be applied to other oceans.

Acknowledgements

We thank Haijin Cao of Hohai University and Xiaolong Huang, who improved this manuscript with helpful comments and fruitful discussions. The numerical simulation is supported by the High Performance Computing Division in the South China Sea Institute of Oceanology. The authors would like to thank GSFC of NASA (http://oceancolor.gsfc.nasa.gov), AVISO+ (https://www.aviso.altimetry.fr), BODC (https://www.bodc.ac.uk), APDRC (http://apdrc.soest.hawaii.edu) for providing a suite of high-resolution satellite data and reanalysis products.

References

Adams K A, Hosegood P, Taylor J R, et al. 2017. Frontal circulation and submesoscale variability during the formation of a Southern Ocean mesoscale eddy. Journal of Physical Oceanography, 47(7): 1737–1753, doi: 10.1175/JPO-D-16-0266.1

Bachman S D, Fox-Kemper B, Taylor J R, et al. 2017. Parameterization of frontal symmetric instabilities. I: theory for resolved fronts. Ocean Modelling, 109: 72–95, doi: 10.1016/j.ocemod.2016.12.003

Boccaletti G, Ferrari R, Fox-Kemper B. 2007. Mixed layer instabilities and restratification. Journal of Physical Oceanography, 37(9): 2228–2250, doi: 10.1175/JPO3101.1

Brannigan L, Marshall D P, Naveira-Garabato A, et al. 2015. The seasonal cycle of submesoscale flows. Ocean Modelling, 92: 69–84, doi: 10.1016/j.ocemod.2015.05.002

Bryden H L, Brady E C. 1989. Eddy momentum and heat fluxes and their effects on the circulation of the equatorial Pacific Ocean. Journal of Marine Research, 47(1): 55–79, doi: 10.1357/002224089785076389

Capet X, McWilliams J C, Molemaker M J, et al. 2008. Mesoscale to submesoscale transition in the California current system. Part II: Frontal processes. Journal of Physical Oceanography, 38(1): 44–64, doi: 10.1175/2007JPO3672.1

Carton J A, Giese B S. 2008. A reanalysis of ocean climate using simple ocean data assimilation (SODA). Monthly Weather Review, 136(8): 2999–3017, doi: 10.1175/2007MWR1978.1

Chelton D B, DeSzoeke R A, Schlax M G, et al. 1998. Geographical variability of the first baroclinic Rossby radius of deformation.

Journal of Physical Oceanography, 28(3): 433–460, doi: 10.1175/1520-0485(1998)028<0433:GVOTFB>2.0.CO;2
Chelton D B, Gaube P, Schlax M G, et al. 2011a. The Influence of nonlinear mesoscale eddies on near-surface oceanic chlorophyll. Science, 334(6054): 328–332, doi: 10.1126/science.1208897
Chelton D B, Schlax M G, Samelson R M. 2011b. Global observations of nonlinear mesoscale eddies. Progress in Oceanography, 91(2): 167–216, doi: 10.1016/j.pocean.2011.01.002
Chen Gengxin, Hou Yijun, Chu Xiaoqing. 2011. Mesoscale eddies in the South China Sea: mean properties, spatiotemporal variability, and impact on thermohaline structure. Journal of Geophysical Research: Oceans, 116(C6): C06018
da Silva A M, Young C C, Levitus S. 1994. Atlas of surface marine data 1994, volume 1: algorithms and procedures. Washington, DC: U. S. Department of Commerce, NOAA, NESDIS
D'Asaro E, Lee C, Rainville L, et al. 2011. Enhanced turbulence and energy dissipation at ocean fronts. Science, 332(6027): 318–322, doi: 10.1126/science.1201515
Dauhajre D P, McWilliams J C, Uchiyama Y. 2017. Submesoscale coherent structures on the continental shelf. Journal of Physical Oceanography, 47(12): 2949–2976, doi: 10.1175/JPO-D-16-0270.1
Dong Changming, McWilliams J C, Liu Yu, et al. 2014. Global heat and salt transports by eddy movement. Nature Communications, 5(1): 3294, doi: 10.1038/ncomms4294
Dong Jihai, Zhong Yisen. 2018. The spatiotemporal features of submesoscale processes in the northeastern South China Sea. Acta Oceanologica Sinica, 37(11): 8–18, doi: 10.1007/s13131-018-1277-2
Dong Jihai, Zhong Yisen. 2020. Submesoscale fronts observed by satellites over the northern South China Sea shelf. Dynamics of Atmospheres and Oceans, 91: 101161, doi: 10.1016/j.dynatmoce.2020.101161
Fox-Kemper B, Ferrari R, Hallberg R. 2008. Parameterization of mixed layer eddies. Part I: theory and diagnosis. Journal of Physical Oceanography, 38(6): 1145–1165, doi: 10.1175/2007JPO3792.1
Gula J, Molemaker M J, McWilliams J C. 2014. Submesoscale cold filaments in the Gulf Stream. Journal of Physical Oceanography, 44(10): 2617–2643, doi: 10.1175/JPO-D-14-0029.1
Guo Lin, Xiu Peng, Chai Fei, et al. 2017. Enhanced chlorophyll concentrations induced by Kuroshio intrusion fronts in the northern South China Sea. Geophysical Research Letters, 44(22): 11565–11572, doi: 10.1002/2017GL075336
Hosegood P J, Gregg M C, Alford M H. 2013. Wind-driven submesoscale subduction at the north Pacific subtropical front. Journal of Geophysical Research: Oceans, 118(10): 5333–5352, doi: 10.1002/jgrc.20385
Hoskins B J. 1974. The role of potential vorticity in symmetric stability and instability. Quarterly Journal of the Royal Meteorological Society, 100(425): 480–482, doi: 10.1002/qj.49710042520
Hoskins B J. 1982. The mathematical theory of frontogenesis. Annual Review of Fluid Mechanics, 14: 131–151, doi: 10.1146/annurev.fl.14.010182.001023
Jing Zhiyou, Fox-Kemper B, Cao Haijin, et al. 2021. Submesoscale fronts and their dynamical processes associated with symmetric instability in the northwest Pacific subtropical ocean. Journal of Physical Oceanography, 51(1): 83–100, doi: 10.1175/JPO-D-20-0076.1
Klein P, Lapeyre G. 2009. The oceanic vertical pump induced by mesoscale and submesoscale turbulence. Annual Review of Marine Science, 1: 351–375, doi: 10.1146/annurev.marine.010908.163704
Klein P, Lapeyre G, Roullet G, et al. 2011. Ocean turbulence at meso and submesoscales: connection between surface and interior dynamics. Geophysical & Astrophysical Fluid Dynamics, 105(4–5): 421–437
Klymak J M, Shearman R K, Gula J, et al. 2016. Submesoscale streamers exchange water on the north wall of the Gulf Stream. Geophysical Research Letters, 43(3): 1226–1233, doi: 10.1002/2015GL067152
Lapeyre G, Klein P. 2006. Dynamics of the upper oceanic layers in terms of surface quasigeostrophy theory. Journal of Physical Oceanography, 36(2): 165–176, doi: 10.1175/JPO2840.1
Large W G, McWilliams J C, Doney S C. 1994. Oceanic vertical mixing: a review and a model with a nonlocal boundary layer parameterization. Reviews of Geophysics, 32(4): 363–403, doi: 10.1029/94RG01872
Lévy M, Klein P, Treguier A M. 2001. Impact of sub-mesoscale physics on production and subduction of phytoplankton in an oligotrophic regime. Journal of Marine Research, 59(4): 535–565, doi: 10.1357/002224001762842181
Li Jiajun, Jiang Xin, Li Gang, et al. 2017. Distribution of picoplankton in the northeastern South China Sea with special reference to the effects of the Kuroshio intrusion and the associated mesoscale eddies. Science of the Total Environment, 589: 1–10, doi: 10.1016/j.scitotenv.2017.02.208
Li Ruihuan, Xu Jie, Cen Xianrong, et al. 2021. Nitrate fluxes induced by turbulent mixing in dipole eddies in an oligotrophic ocean. Limnology and Oceanography, 66(7): 2842–2854, doi: 10.1002/lno.11794
Lin Hongyang, Liu Zhiyu, Hu Jianyu, et al. 2020. Characterizing meso- to submesoscale features in the South China Sea. Progress in Oceanography, 188: 102420, doi: 10.1016/j.pocean.2020.102420
Mahadevan A. 2016. The impact of submesoscale physics on primary productivity of plankton. Annual Review of Marine Science, 8: 161–184, doi: 10.1146/annurev-marine-010814-015912
Martin A P. 2003. Phytoplankton patchiness: the role of lateral stirring and mixing. Progress in Oceanography, 57(2): 125–174, doi: 10.1016/S0079-6611(03)00085-5
Mason E, Pascual A, McWilliams J C. 2014. A new sea surface height-based code for oceanic mesoscale eddy tracking. Journal of Atmospheric and Oceanic Technology, 31(5): 1181–1188, doi: 10.1175/JTECH-D-14-00019.1
McGillicuddy D J Jr. 2016. Mechanisms of physical-biological-biogeochemical interaction at the oceanic mesoscale. Annual Review of Marine Science, 8: 125–159, doi: 10.1146/annurev-marine-010814-015606
McGillicuddy D J Jr, Anderson L A, Doney S C, et al. 2003. Eddy-driven sources and sinks of nutrients in the upper ocean: results from a 0.1° resolution model of the North Atlantic. Global Biogeochemical Cycles, 17(2): 1035
McWilliams J C. 2017. Submesoscale surface fronts and filaments: secondary circulation, buoyancy flux, and frontogenesis. Journal of Fluid Mechanics, 823: 391–432, doi: 10.1017/jfm.2017.294
McWilliams J C, Colas F, Molemaker M J. 2009a. Cold filamentary intensification and oceanic surface convergence lines. Geophysical Research Letters, 36(18): L18602, doi: 10.1029/2009GL039402
McWilliams J C, Gula J, Molemaker M J, et al. 2015. Filament frontogenesis by boundary layer turbulence. Journal of Physical Oceanography, 45(8): 1988–2005, doi: 10.1175/JPO-D-14-0211.1
McWilliams J C, Molemaker M J, Olafsdottir E I. 2009b. Linear fluctuation growth during frontogenesis. Journal of Physical Oceanography, 39(12): 3111–3129, doi: 10.1175/2009JPO4186.1
Munk W, Armi L, Fischer K, et al. 2000. Spirals on the sea. Proceedings of the Royal Society A: Mathematical, Physical and Engineering Sciences, 456(1997): 1217–1280
Nan Feng, Xue Huijie, Xiu Peng, et al. 2011. Oceanic eddy formation and propagation southwest of Taiwan. Journal of Geophysical Research: Oceans, 116(C12): C12045, doi: 10.1029/2011JC007386
Omand M M, D'Asaro E A, Lee C M, et al. 2015. Eddy-driven subduction exports particulate organic carbon from the spring bloom. Science, 348(6231): 222–225, doi: 10.1126/science.1260062
Penven P, Debreu L, Marchesiello P, et al. 2006. Evaluation and application of the ROMS 1-way embedding procedure to the central california upwelling system. Ocean Modelling, 12(1–2): 157–187, doi: 10.1016/j.ocemod.2005.05.002
Qiu Bo, Chen Shuiming. 2010. Interannual variability of the North Pacific Subtropical Countercurrent and its associated mesoscale

eddy field. Journal of Physical Oceanography, 40(1): 213–225, doi: 10.1175/2009JPO4285.1

Read J F, Pollard R T, Allen J T. 2007. Sub-mesoscale structure and the development of an eddy in the subantarctic front north of the Crozet Islands. Deep-Sea Research Part II: Topical Studies in Oceanography, 54(18–20): 1930–1948, doi: 10.1016/j.dsr2.2007.06.013

Risien C M, Chelton D B. 2008. A global climatology of surface wind and wind stress fields from eight years of QuikSCAT scatterometer data. Journal of Physical Oceanography, 38(11): 2379–2413, doi: 10.1175/2008JPO3881.1

Shakespeare C J, Taylor J R. 2013. A generalized mathematical model of geostrophic adjustment and frontogenesis: uniform potential vorticity. Journal of Fluid Mechanics, 736: 366–413, doi: 10.1017/jfm.2013.526

Shchepetkin A F, McWilliams J C. 2005. The regional oceanic modeling system (ROMS): a split-explicit, free-surface, topography-following-coordinate oceanic model. Ocean Modelling, 9(4): 347–404, doi: 10.1016/j.ocemod.2004.08.002

Spall M A. 1995. Frontogenesis, subduction, and cross-front exchange at upper ocean fronts. Journal of Geophysical Research: Oceans, 100(C2): 2543–2557, doi: 10.1029/94JC02860

Stone P H. 1966. On non-geostrophic baroclinic stability. Journal of the Atmospheric Sciences, 23(4): 390–400, doi: 10.1175/1520-0469(1966)023<0390:ONGBS>2.0.CO;2

Su Zhan, Torres H, Klein P, et al. 2020. High-frequency submesoscale motions enhance the upward vertical heat transport in the global ocean. Journal of Geophysical Research: Oceans, 125(9): e2020JC016544

Su Zhan, Wang Jinbo, Klein P, et al. 2018. Ocean submesoscales as a key component of the global heat budget. Nature Communications, 9(1): 775, doi: 10.1038/s41467-018-02983-w

Sullivan P P, McWilliams J C. 2018. Frontogenesis and frontal arrest of a dense filament in the oceanic surface boundary layer. Journal of Fluid Mechanics, 837: 341–380, doi: 10.1017/jfm.2017.833

Tang Qunshu, Jing Zhiyou, Lin Jianmin, et al. 2021. Diapycnal mixing in the subthermocline of the Mariana Ridge from high-resolution seismic images. Journal of Physical Oceanography, 51(4): 1283–1300, doi: 10.1175/JPO-D-20-0120.1

Tarry D R, Essink S, Pascual A, et al. 2021. Frontal convergence and vertical velocity measured by drifters in the Alboran Sea. Journal of Geophysical Research: Oceans, 126(4): e2020JC016614

Taylor J R, Ferrari R. 2009. On the equilibration of a symmetrically unstable front via a secondary shear instability. Journal of Fluid Mechanics, 622: 103–113, doi: 10.1017/S0022112008005272

Thomas L N, Taylor J R, Ferrari R, et al. 2013. Symmetric instability in the Gulf Stream. Deep-Sea Research Part II: Topical Studies in Oceanography, 91: 96–110, doi: 10.1016/j.dsr2.2013.02.025

Thompson A F, Lazar A, Buckingham C, et al. 2016. Open-ocean submesoscale motions: a full seasonal cycle of mixed layer instabilities from gliders. Journal of Physical Oceanography, 46(4): 1285–1307, doi: 10.1175/JPO-D-15-0170.1

Wang Dongxiao, Xu Hongzhou, Lin Jing, et al. 2008. Anticyclonic eddies in the northeastern South China Sea during winter 2003/2004. Journal of Oceanography, 64(6): 925–935, doi: 10.1007/s10872-008-0076-3

Woodruff S D, Worley S J, Lubker S J, et al. 2011. ICOADS Release 2.5: extensions and enhancements to the surface marine meteorological archive. International Journal of Climatology, 31(7): 951–967, doi: 10.1002/joc.2103

Yang Qingxuan, Nikurashin M, Sasaki H, et al. 2019. Dissipation of mesoscale eddies and its contribution to mixing in the northern South China Sea. Scientific Reports, 9(1): 556, doi: 10.1038/s41598-018-36610-x

Yang Qingxuan, Zhao Wei, Liang Xinfeng, et al. 2017. Elevated mixing in the periphery of mesoscale eddies in the South China Sea. Journal of Physical Oceanography, 47(4): 895–907, doi: 10.1175/JPO-D-16-0256.1

Zhang Yanwei, Liu Zhifei, Zhao Yulong, et al. 2014. Mesoscale eddies transport deep-sea sediments. Scientific Reports, 4: 5937

Zhang Zhengguang, Qiu Bo. 2020. Surface chlorophyll enhancement in mesoscale eddies by submesoscale spiral bands. Geophysical Research Letters, 47(14): e2020GL088820

Zhang Zhiwei, Tian Jiwei, Qiu Bo, et al. 2016. Observed 3D structure, generation, and dissipation of oceanic mesoscale eddies in the South China Sea. Scientific Reports, 6(1): 24349, doi: 10.1038/srep24349

Zhang Zhiwei, Zhang Yuchen, Qiu Bo, et al. 2020. Spatiotemporal characteristics and generation mechanisms of submesoscale currents in the northeastern South China Sea revealed by numerical simulations. Journal of Geophysical Research: Oceans, 125(2): e2019JC015404

Zheng Quanan, Xie Lingling, Xiong Xuejun, et al. 2020. Progress in research of submesoscale processes in the South China Sea. Acta Oceanologica Sinica, 39(1): 1–13, doi: 10.1007/s13131-019-1521-4

Zhong Yisen, Bracco A, Tian Jiwei, et al. 2017. Observed and simulated submesoscale vertical pump of an anticyclonic eddy in the South China Sea. Scientific Reports, 7(1): 44011, doi: 10.1038/srep44011